Frontiers of Information Technology & Electronic Engineering
www.jzus.zju.edu.cn; engineering.cae.cn; www.springerlink.com
ISSN 2095-9184 (print); ISSN 2095-9230 (online)
E-mail: jzus@zju.edu.cn

Modeling of a dynamic dual-input dual-output fast steering mirror system*

Hong SONG[1], Jia-heng ZHANG[1], Ping YANG[†‡2], Hao-cai HUANG[1], Shu-yue ZHAN[1], Teng-jun LIU[1], Yi-lu GUO[1], Hang-zhou WANG[1], Hui HUANG[1], Quan-quan MU[3], Mei-fen FANG[4], Ming-yuan YANG[5]

([1]*Ocean College, Zhejiang University, Zhoushan 316021, China*)

([2]*School of Digital Media & Design, Hangzhou Dianzi University, Hangzhou 310018, China*)

([3]*State Key Laboratory of Applied Optics, Changchun Institute of Optics, Fine Mechanics and Physics, Chinese Academy of Sciences, Jilin 130033, China*)

([4]*Blue-Science Opto-Electronics Co. Ltd., Hangzhou 310018, China*)

([5]*Core Tomorrow Science & Technology Co. Ltd., Harbin 150080, China*)

[†]E-mail: yangping@hdu.edu.cn

Received May 1, 2016; Revision accepted Aug. 15, 2016; Crosschecked Oct. 18, 2017

Abstract: A modeling method is proposed for a dynamic fast steering mirror (FSM) system with dual inputs and dual outputs. A physical model of the FSM system is derived based on first principles, describing the dynamics and coupling between the inputs and outputs of the FSM system. The physical model is then represented in a state-space form. Unknown parameters in the state-space model are identified by the subspace identification algorithm, based on the measured input-output data of the FSM system. The accuracy of the state-space model is evaluated by comparing the model estimates with measurements. The variance-accounted-for value of the state-space model is better than 97%, not only for the modeling data but also for the validation data set, indicating high accuracy of the model. Comparison is also made between the proposed dynamic model and the conventional static model, where improvement in model accuracy is clearly observed. The model identified by the proposed method can be used for optimal controller design for closed-loop FSM systems. The modeling method is also applicable to FSM systems with similar structures.

Key words: Fast steering mirror; Dynamic system; Input-output coupling, Physical modeling; Subspace identification

https://doi.org/10.1631/FITEE.1601221 **CLC number:** TP273

1 Introduction

Fast steering mirrors (FSMs) have been widely used in various applications, e.g., telescope systems (Cao *et al.* 2009; 2012), retina imaging (Mu *et al.*, 2008), and wireless laser communication (Raj *et al.*, 2015), for rapid and accurate beam tracking and alignment.

FSM is generally composed of a plane mirror and multiple actuators supporting the mirror (Lu *et al.*, 2013). The actuators deform in response to applied driving voltages or currents. Hence, the orientation of the mirror surface and the direction of the reflected beam are changed (Portillo *et al.*, 2001). The direction of the beam is measured, for instance, by position sensitive devices (PSDs) or cameras. The measurement is then fed to the controller and a

‡ Corresponding author

* Project supported by the National Natural Science Foundation of China (No. 11304278) and the National High-Tech R&D Program (863) of China (No. 2014AA093400)

ORCID: Hong SONG, http://orcid.org/0000-0002-1000-4764

control signal is generated such that the beam direction is controlled in real time (Arancibia *et al.*, 2006).

Although proportional-integral-derivative (PID) controllers have been commonly used for control of closed-loop FSM systems (Tang *et al.*, 2011; Alvi *et al.*, 2014; Yu *et al.*, 2015), model-based control approaches (Hinnen *et al.*, 2008; Song *et al.*, 2011) have shown great potential to further improve the performance of closed-loop FSM systems. In such a case, an accurate model of the open-loop FSM system is crucial for model-based controller design. However, as the sampling rate of the position sensor increases (e.g., to the order of kHz), the dynamics of the FSM becomes evident (Wang and Rao, 2015). Furthermore, as the inputs to the FSM system (e.g., control signals to the actuators) do not necessarily have a one-on-one correspondence with the sensor outputs (e.g., displacement of the beam spot in the PSD), the input and output channels of the FSM system are coupled, which adds to the difficulty in modeling the dynamics of the FSM system (Hei *et al.*, 2015).

A physical model of an FSM was derived in Hei *et al.* (2015), where the dynamics and coupling of the FSM were considered. Coefficients in the model were calculated from physical parameters of each component. A dynamic model of an FSM system was proposed in Wang and Rao (2015) in the form of a transfer function, describing the dynamic transfer from the control signal of one actuator to the displacement of a light spot in the sensor. Coefficients in the transfer function were estimated from the input-output data of the FSM system. An artificial neural network was also used in the modeling and controller design of an FSM system and good correction performance was achieved in a 500-m free-space optical communication experiment (Raj *et al.*, 2015).

Since deformable mirrors (DMs) used in adaptive optics (AO) systems are similar to FSMs in the sense that DMs also exhibit dynamics and input-output coupling behavior, the methods for DM modeling can be used for modeling of the FSM system. For instance, a state-space model describing the dynamics and coupling in the AO system has been built and used for model-based controller design (Song *et al.*, 2011). The coefficients in the state-space model were identified with high accuracy by a subspace identification approach (Verhaegen and Verdult, 2007; Chiuso *et al.*, 2010), based on the input-output data of the AO system.

As physical modeling helps gain insight into the mechanism of the system while data-driven identification methods (e.g., subspace identification) are able to provide numerical models with high accuracy, these two methods are combined in this study to model a dynamic input-output coupled FSM system, by taking advantage of both methods. A model of the FSM system is achieved with both physical insight and high numerical accuracy, which can be used for model-based controller design in the future. Furthermore, the modeling method proposed is suitable not only for the FSM system investigated in this study, but also for other FSM systems with similar structures.

2 System description

A schematic of the FSM system under investigation is illustrated in Fig. 1. The incident beam is reflected by the FSM and transmitted to the PSD. The sensor signal is filtered and amplified. The coordinates of the beam centroid are calculated and the displacement of the beam spot is determined. In closed-loop operation, the control signal of the FSM is generated by a feedback controller, based on the displacement measurement. However, in this study, we consider only modeling of the open-loop FSM system (as denoted by the dashed box) with the feedback controller absent.

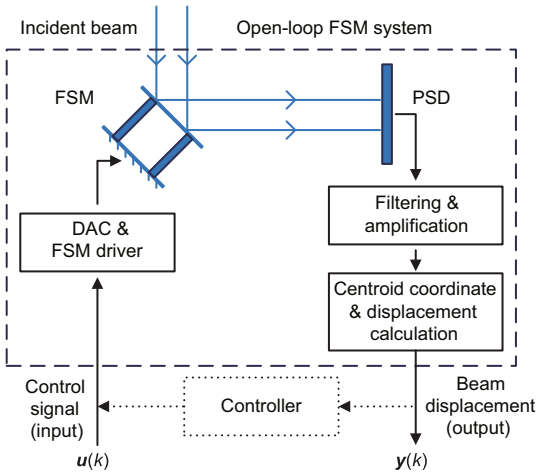

Fig. 1 Schematic of a closed-loop fast steering mirror (FSM) system. The open-loop FSM system included in the dashed box is modeled in this study, with the control signal as the input and the displacement of the beam spot in the PSD as the output

The input of the open-loop FSM system is the control signal to the FSM, denoted as $\boldsymbol{u}(k)$ for discrete time k. The output is the displacement of the beam spot, denoted as $\boldsymbol{y}(k)$. Because the FSM has two pairs of actuators in different structures (i.e., two control channels) and the PSD provides the displacements of the beam spot in both horizontal and vertical directions, the control signal $\boldsymbol{u}(k)$ and sensor signal $\boldsymbol{y}(k)$ are both two-dimensional vectors, i.e., $\boldsymbol{u}(k) = [u_1(k), u_2(k)]^{\mathrm{T}} \in \mathbb{R}^2$ and $\boldsymbol{y}(k) = [y_1(k), y_2(k)]^{\mathrm{T}} \in \mathbb{R}^2$. Here $u_1(k)$ and $u_2(k)$ are control signals to two actuator pairs; $y_1(k)$ and $y_2(k)$ are displacements of the beam spot in the horizontal and vertical directions, respectively.

3 Modeling by physical principles

The geometric configuration of the FSM and PSD is shown in Fig. 2a, where the incident beam is reflected by the FSM and the displacement of the reflected beam spot is measured by the PSD. When the mirror surface is deflected, the beam spot has a displacement of x_{d} in the horizontal direction of the PSD (denoted as x_{c}) and a displacement of y_{d} in the vertical direction (denoted as y_{c}).

The distribution of actuators in the FSM is shown in Fig. 2b, where $(\mathrm{a}_1, \mathrm{a}_2)$ and $(\mathrm{b}_1, \mathrm{b}_2)$ denote two pairs of actuators in different structures (i.e., push-and-pull). When control signals are applied, actuators deform in pairs (Fig. 2c). The coordinate axis x'_{c} is defined along the actuator pair $(\mathrm{a}_1, \mathrm{a}_2)$ and y'_{c} is along the pair $(\mathrm{b}_1, \mathrm{b}_2)$. In most cases, there is an angle between axes x_{c} and x'_{c} (denoted as θ_1), such that the deflection of one pair of actuators leads to spot movement in both directions of x_{c} and y_{c} in the PSD. Hence, coupling exists between the control signals to the actuator pairs and spot displacement.

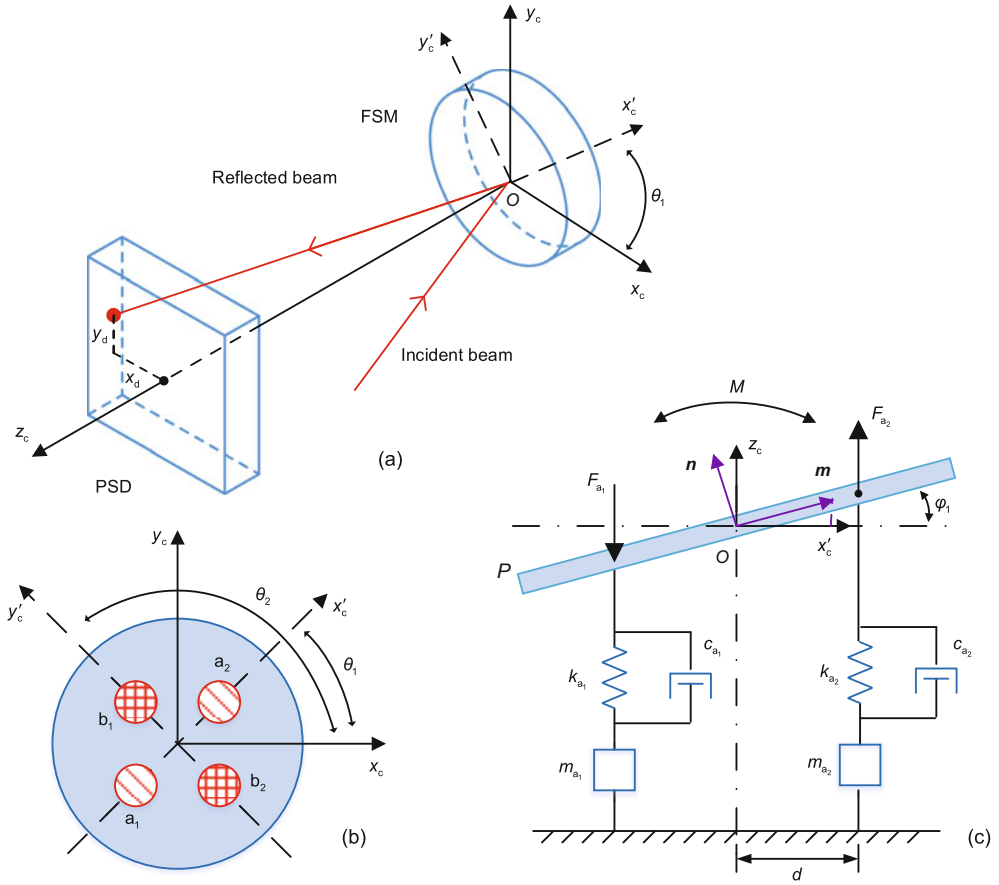

Fig. 2 Operation principle of an FSM: (a) geometric configuration of the FSM and PSD in Cartesian coordinates; (b) distribution of actuators in the FSM (four actuators are structured in two pairs pushing and pulling the mirror surface in the x'_{c}- and y'_{c}-direction); (c) mirror surface deflected by a pair of push-pull actuators $(\mathrm{a}_1, \mathrm{a}_2)$ in the x'_{c}-direction

3.1 Modeling of the fast steering mirror

To see how the mirror surface deflects with control signals, the cross section of the FSM is depicted in Fig. 2c for the actuator pair $(\mathrm{a}_1, \mathrm{a}_2)$. Here, φ_1 is the deflection angle of the FSM when control signal u_1 is applied to the actuator pair $(\mathrm{a}_1, \mathrm{a}_2)$. Plane P represents the mirror surface after deflection. The forces generated by two actuators are denoted as F_{a_1} and F_{a_2}.

Without lose of generality, each actuator is modeled as a second-order mass-damper system. The relationship between the mirror's torque (denoted as M) and the deflection angle φ_1 can be written as (Raj *et al.*, 2015; Wang and Rao, 2015)

$$\begin{aligned} M =&[J + (m_{\mathrm{a}_1} + m_{\mathrm{a}_2})d^2]\ddot{\varphi}_1 + (c_{\mathrm{a}_1} + c_{\mathrm{a}_2})d^2\dot{\varphi}_1 \\ &+ (k_{\mathrm{a}_1} + k_{\mathrm{a}_2})d^2\varphi_1, \end{aligned} \tag{1}$$

where J is the moment of inertia, d the distance between the actuator and the center of the mirror surface, m_{a_1} and m_{a_2} the masses, c_{a_1} and c_{a_2} the damping coefficients, and k_{a_1} and k_{a_2} the elastic coefficients of the two actuators.

Because the two actuators are of the same type, it is reasonable to assume that the forces generated by two actuators have the same magnitude but in the opposite direction, i.e., $F_{\mathrm{a}_1} = -F_{\mathrm{a}_2}$. The torque M and the force F_{a_1} are related by

$$M = \underbrace{2F_{\mathrm{a}_1}}_{F_1} \cdot d, \tag{2}$$

where $F_1 = 2F_{\mathrm{a}_1}$ is an intermediate variable. Combining Eqs. (1) and (2), we have

$$F_1 = 2F_{\mathrm{a}_1} = m_1\ddot{\varphi}_1 + c_1\dot{\varphi}_1 + k_1\varphi_1, \tag{3}$$

where $m_1 = [J+(m_{\mathrm{a}_1}+m_{\mathrm{a}_2})d^2]/d$, $c_1 = (c_{\mathrm{a}_1}+c_{\mathrm{a}_2})d$, and $k_1 = (k_{\mathrm{a}_1} + k_{\mathrm{a}_2})d$ denote the equivalent mass, equivalent damping coefficient, and equivalent elastic coefficient of the actuator pair $(\mathrm{a}_1, \mathrm{a}_2)$, respectively.

The force F_1 generated by the actuator pair is determined by the control signal u_1 as

$$F_1 = p_1 u_1, \tag{4}$$

where p_1 is a coefficient representing the transfer from the control signal to actuator force. Therefore, the control signal u_1 and deflection angle φ_1 are related as

$$u_1 = \frac{1}{p_1}(m_1\ddot{\varphi}_1 + c_1\dot{\varphi}_1 + k_1\varphi_1). \tag{5}$$

Similar to Eq. (5), we have

$$u_2 = \frac{1}{p_2}(m_2\ddot{\varphi}_2 + c_2\dot{\varphi}_2 + k_2\varphi_2) \tag{6}$$

for the connection between the control signal u_2 to the pair $(\mathrm{b}_1, \mathrm{b}_2)$ and resultant deflection angle φ_2. Here, p_2 is a coefficient, and m_2, c_2, and k_2 denote the equivalent mass, equivalent damping coefficient, and equivalent elastic coefficient of the actuator pair $(\mathrm{b}_1, \mathrm{b}_2)$, respectively.

FSM's deflections in directions of x'_{c} and y'_{c} are manipulated by actuator pairs $(\mathrm{a}_1, \mathrm{a}_2)$ and $(\mathrm{b}_1, \mathrm{b}_2)$ independently. When two actuator pairs are excited simultaneously, the total angular deflections in directions of x'_{c} and y'_{c} are determined by Eqs. (5) and (6), respectively.

3.2 Modeling of the FSM-PSD system

Referring to Fig. 2c, two vectors are defined, namely $\boldsymbol{n}$ and $\boldsymbol{m}$. Note that $\boldsymbol{n}$ is the unit normal vector of plane P, $\boldsymbol{m}$ is a unit vector in plane P, and the projection of $\boldsymbol{m}$ on plane $x_{\mathrm{c}}oy_{\mathrm{c}}$ is in the axis x'_{c}. When the mirror surface is in its nominal position (i.e., $\varphi_1 = 0$), the projections of $\boldsymbol{m}$ in the axes x_{c}, y_{c}, and z_{c} are $\cos\theta_1$, $\sin\theta_1$, and 0, respectively. As the mirror surface is deflected by φ_1 from its nominal position, the projections of $\boldsymbol{m}$ in the axes x_{c}, y_{c}, and z_{c} change to $\cos\varphi_1\cos\theta_1$, $\cos\varphi_1\sin\theta_1$, and $\sin\varphi_1$, respectively. Therefore, $\boldsymbol{m}$ can be represented as

$$\boldsymbol{m} = (\cos\varphi_1\cos\theta_1,\ \cos\varphi_1\sin\theta_1,\ \sin\varphi_1) \tag{7}$$

in the coordinate system defined by x_{c}, y_{c}, and z_{c}.

Since vectors $\boldsymbol{n}$ and $\boldsymbol{m}$ are orthogonal to each other, i.e., $\boldsymbol{n} \perp \boldsymbol{m}$, $\boldsymbol{n}$ can be represented as

$$\boldsymbol{n} = (-\sin\varphi_1\cos\theta_1,\ -\sin\varphi_1\sin\theta_1,\ \cos\varphi_1). \tag{8}$$

Hence, each point in plane P satisfies

$$-\sin\varphi_1\cos\theta_1\cdot x_{\mathrm{p}} - \sin\varphi_1\sin\theta_1\cdot y_{\mathrm{p}} + \cos\varphi_1\cdot z_{\mathrm{p}} = 0, \tag{9}$$

where x_{p}, y_{p}, and z_{p} are coordinates of the point in plane P.

The projection of deflection angle φ_1 in axis x_{c} (denoted as φ_{1x}) can be calculated by setting $y_{\mathrm{p}} = 0$ in Eq. (9), i.e.,

$$\tan\varphi_{1x} = \frac{z_{\mathrm{p}}}{x_{\mathrm{p}}} = \frac{\sin\varphi_1\cos\theta_1}{\cos\varphi_1} = \tan\varphi_1\cos\theta_1. \tag{10}$$

Similarly, the projection of deflection angle φ_1 in axis y_c can be calculated by taking $x_p = 0$ in Eq. (9) as

$$\tan\varphi_{1y} = \frac{z_p}{y_p} = \frac{\sin\varphi_1 \sin\theta_1}{\cos\varphi_1} = \tan\varphi_1 \sin\theta_1. \quad (11)$$

Because FSMs are used mainly for precise beam alignment, angle φ_1 is usually of the order of mrad (1 mrad=10^{-3} rad); e.g., the FSM used in our experimental setup has a range of ±6 mrad. It is approximated that

$$\tan\varphi_1 \approx \varphi_1,\ \tan\varphi_{1x} \approx \varphi_{1x},\ \tan\varphi_{1y} \approx \varphi_{1y}. \quad (12)$$

Therefore, we have

$$\begin{cases} \varphi_{1x} \approx \varphi_1 \cos\theta_1, \\ \varphi_{1y} \approx \varphi_1 \sin\theta_1. \end{cases} \quad (13)$$

When the actuator pair (b_1, b_2) is excited, the FSM is deflected along axis y_c'. Denote the angle of deflection as φ_2. Similar to Eq. (13), the projection of φ_2 in axes x_c and y_c can be represented as

$$\begin{cases} \varphi_{2x} \approx \varphi_2 \cos\theta_2, \\ \varphi_{2y} \approx \varphi_2 \sin\theta_2. \end{cases} \quad (14)$$

Since we have $\theta_2 = \theta_1 + \dfrac{\pi}{2}$, Eq. (14) can be rewritten as

$$\begin{cases} \varphi_{2x} = -\varphi_2 \sin\theta_1, \\ \varphi_{2y} = \varphi_2 \cos\theta_1. \end{cases} \quad (15)$$

Combining Eqs. (13) and (15), when two pairs of actuators are excited simultaneously, FSM's angular deflection in the directions of x_c and y_c can be written as

$$\begin{cases} \varphi_x = \varphi_{1x} + \varphi_{2x} = \varphi_1 \cos\theta_1 - \varphi_2 \sin\theta_1, \\ \varphi_y = \varphi_{1y} + \varphi_{2y} = \varphi_1 \sin\theta_1 + \varphi_2 \cos\theta_1. \end{cases} \quad (16)$$

In most cases, the distance between the FSM and the PSD (denoted as L) is much larger than the displacement of the spot in the PSD. The displacements x_d and y_d can be approximated as

$$\begin{cases} x_d \approx 2L\varphi_x, \\ y_d \approx 2L\varphi_y. \end{cases} \quad (17)$$

Setting $H = 2L$ and substituting Eq. (16) into Eq. (17), we have

$$\begin{cases} x_d = H\cos\theta_1 \cdot \varphi_1 - H\sin\theta_1 \cdot \varphi_2, \\ y_d = H\sin\theta_1 \cdot \varphi_1 - H\cos\theta_1 \cdot \varphi_2. \end{cases} \quad (18)$$

The connection among the control signal, deflection angle, and spot displacement in the PSD has been revealed so far in Eqs. (5), (6), and (18). Dynamics in the FSM and the coupling between control signals and spot displacement are clearly visible.

3.3 Representation of the FSM system in state-space form

To have an accurate model which can be used for controller design for the FSM, parameters in Eqs. (5), (6), and (18) need to be known with high accuracy, which is impractical in many cases. Alternatively, a numerical model of the FSM system can be identified based on the input-output data of the system using a subspace identification method.

In subspace identification, the FSM system is represented in state-space form as (Verhaegen and Verdult, 2007)

$$\begin{cases} \boldsymbol{x}(k+1) = \boldsymbol{A}\boldsymbol{x}(k) + \boldsymbol{B}\boldsymbol{u}(k), \\ \boldsymbol{y}(k) = \boldsymbol{C}\boldsymbol{x}(k) + \boldsymbol{D}\boldsymbol{u}(k) + \boldsymbol{v}(k), \end{cases} \quad (19)$$

where $\boldsymbol{u}(k) \in \mathbb{R}^2$ is the input to the system (i.e., control signal), $\boldsymbol{y}(k) \in \mathbb{R}^2$ is the output of the system (i.e., spot displacement), $\boldsymbol{x}(k) \in \mathbb{R}^n$ is the state vector, n is the dimension of the state vector, and $\boldsymbol{v}(k) \in \mathbb{R}^2$ is the measurement noise.

The dynamics of the system are embraced in the system matrix $\boldsymbol{A} \in \mathbb{R}^{n\times n}$, input matrix $\boldsymbol{B} \in \mathbb{R}^{n\times 2}$, and output matrix $\boldsymbol{C} \in \mathbb{R}^{2\times n}$. The matrix $\boldsymbol{D} \in \mathbb{R}^{2\times 2}$ represents the direct transfer from the input to the output.

The transfer function $T(z)$ of the system can also be calculated from the state-space form as

$$\boldsymbol{T}(z) = \frac{\boldsymbol{Y}(z)}{\boldsymbol{U}(z)} = \boldsymbol{C}(z\boldsymbol{I} - \boldsymbol{A})^{-1}\boldsymbol{B} + \boldsymbol{D}, \quad (20)$$

where z is the z-transform operator. $U(z)$ and $Y(z)$ are the z-transforms of $\boldsymbol{u}(k)$ and $\boldsymbol{y}(k)$, respectively. For static models, matrices $\boldsymbol{A}$, $\boldsymbol{B}$, and $\boldsymbol{C}$ are all zero, giving $\boldsymbol{y}(k) = \boldsymbol{D}\boldsymbol{u}(k)$.

To see how the physical model is connected with the state-space model, Eqs. (5), (6), and (18) are

written in the state-space form as

$$\begin{cases} \underbrace{\begin{bmatrix} \ddot{\varphi}_1 \\ \ddot{\varphi}_2 \\ \dot{\varphi}_1 \\ \dot{\varphi}_2 \end{bmatrix}}_{\dot{\boldsymbol{x}}} = \underbrace{\begin{bmatrix} -\frac{c_1}{m_1} & 0 & -\frac{k_1}{m_1} & 0 \\ 0 & -\frac{c_2}{m_2} & 0 & -\frac{k_2}{m_2} \\ 1 & 0 & 0 & 0 \\ 0 & 1 & 0 & 0 \end{bmatrix}}_{\boldsymbol{A}} \cdot \underbrace{\begin{bmatrix} \dot{\varphi}_1 \\ \dot{\varphi}_2 \\ \varphi_1 \\ \varphi_2 \end{bmatrix}}_{\boldsymbol{x}} + \underbrace{\begin{bmatrix} \frac{p_1}{m_1} & 0 \\ 0 & \frac{p_2}{m_2} \\ 0 & 0 \\ 0 & 0 \end{bmatrix}}_{\boldsymbol{B}} \cdot \underbrace{\begin{bmatrix} u_1 \\ u_2 \end{bmatrix}}_{\boldsymbol{u}}, \\ \underbrace{\begin{bmatrix} x_\mathrm{d} \\ y_\mathrm{d} \end{bmatrix}}_{\boldsymbol{y}} = \underbrace{\begin{bmatrix} 0 & 0 & H\cos\theta_1 & -H\sin\theta_1 \\ 0 & 0 & H\sin\theta_1 & -H\cos\theta_1 \end{bmatrix}}_{\boldsymbol{C}} \cdot \underbrace{\begin{bmatrix} \dot{\varphi}_1 \\ \dot{\varphi}_2 \\ \varphi_1 \\ \varphi_2 \end{bmatrix}}_{\boldsymbol{x}}, \end{cases} \tag{21}$$

where $\boldsymbol{x} = [\dot{\varphi}_1, \dot{\varphi}_2, \varphi_1, \varphi_2]^\mathrm{T}$ is the system variable. $\boldsymbol{u} = [u_1, u_2]^\mathrm{T}$ and $\boldsymbol{y} = [x_\mathrm{d}, y_\mathrm{d}]^\mathrm{T}$ represent the input and output of the system, respectively. Dynamics of the system are clearly visible in matrix $\boldsymbol{A}$. The input-output coupling is visible in matrix $\boldsymbol{C}$. Note that the state-space model in Eq. (21) is in continuous time and the goal is to show mainly the connection between the physical model and the state-space model. During the identification process, system matrices $\boldsymbol{A}$, $\boldsymbol{B}$, $\boldsymbol{C}$, and $\boldsymbol{D}$ in Eq. (19) are solved from the input-output data $\boldsymbol{u}(k)$ and $\boldsymbol{y}(k)$.

4 Principles on subspace identification

According to Eq. (19), the state vector $\boldsymbol{x}(k)$ at discrete time k can be described as

$$\boldsymbol{x}(k) = \boldsymbol{A}^k \boldsymbol{x}(0) + \sum_{i=0}^{k-1} \boldsymbol{A}^{k-i-1} \boldsymbol{B} \boldsymbol{u}(i), \tag{22}$$

where $\boldsymbol{x}(0)$ denotes the initial state. Substituting Eq. (22) into Eq. (19) yields

$$\begin{aligned} \boldsymbol{y}(k) =& \boldsymbol{C}\boldsymbol{A}^k \boldsymbol{x}(0) + \sum_{i=0}^{k-1} \boldsymbol{C}\boldsymbol{A}^{k-i-1} \boldsymbol{B}\boldsymbol{u}(i) \\ &+ \boldsymbol{D}\boldsymbol{u}(k) + \boldsymbol{v}(k). \end{aligned} \tag{23}$$

Consider a given set of input and output vectors of size M, namely $\boldsymbol{u}(k)$ and $\boldsymbol{y}(k)$, $k = 0, 1, \ldots, M-1$. The first M elements of $\boldsymbol{y}(k)$ can be written in matrix form as (Jansson and Wahlberg, 1996; Verhaegen and Verdult, 2007)

$$\begin{aligned} \begin{bmatrix} \boldsymbol{y}(0) \\ \boldsymbol{y}(1) \\ \vdots \\ \boldsymbol{y}(M-1) \end{bmatrix} =& \begin{bmatrix} \boldsymbol{C} \\ \boldsymbol{C}\boldsymbol{A} \\ \vdots \\ \boldsymbol{C}\boldsymbol{A}^{M-1} \end{bmatrix} \boldsymbol{x}(0) \\ &+ \begin{bmatrix} \boldsymbol{D} & \boldsymbol{0} & \cdots & \boldsymbol{0} \\ \boldsymbol{C}\boldsymbol{B} & \boldsymbol{D} & \cdots & \boldsymbol{0} \\ \vdots & \vdots & & \vdots \\ \boldsymbol{C}\boldsymbol{A}^{M-2}\boldsymbol{B} & \boldsymbol{C}\boldsymbol{A}^{M-3}\boldsymbol{B} & \cdots & \boldsymbol{0} \end{bmatrix} \begin{bmatrix} \boldsymbol{u}(0) \\ \boldsymbol{u}(1) \\ \vdots \\ \boldsymbol{u}(M-1) \end{bmatrix} \\ &+ \begin{bmatrix} \boldsymbol{v}(0) \\ \boldsymbol{v}(1) \\ \vdots \\ \boldsymbol{v}(M-1) \end{bmatrix}. \end{aligned} \tag{24}$$

By defining

$$\boldsymbol{\Gamma}_M = \begin{bmatrix} \boldsymbol{C} \\ \boldsymbol{C}\boldsymbol{A} \\ \vdots \\ \boldsymbol{C}\boldsymbol{A}^{M-1} \end{bmatrix}, \tag{25}$$

$$\boldsymbol{H}_M = \begin{bmatrix} \boldsymbol{D} & \boldsymbol{0} & \cdots & \boldsymbol{0} \\ \boldsymbol{C}\boldsymbol{B} & \boldsymbol{D} & \cdots & \boldsymbol{0} \\ \vdots & \vdots & & \vdots \\ \boldsymbol{C}\boldsymbol{A}^{M-2}\boldsymbol{B} & \boldsymbol{C}\boldsymbol{A}^{M-3}\boldsymbol{B} & \cdots & \boldsymbol{D} \end{bmatrix}, \tag{26}$$

and

$$\boldsymbol{Y}_M(0) = [\boldsymbol{y}(0), \boldsymbol{y}(1), \ldots, \boldsymbol{y}(M-1)]^\mathrm{T}, \tag{27}$$

$$\boldsymbol{U}_M(0) = [\boldsymbol{u}(0), \boldsymbol{u}(1), \ldots, \boldsymbol{u}(M-1)]^\mathrm{T}, \tag{28}$$

$$\boldsymbol{V}_M(0) = [\boldsymbol{v}(0), \boldsymbol{v}(1), \ldots, \boldsymbol{v}(M-1)]^\mathrm{T}, \tag{29}$$

Eq. (24) can be written in a compact form as

$$\boldsymbol{Y}_M(0) = \boldsymbol{\Gamma}_M \boldsymbol{x}(0) + \boldsymbol{H}_M \boldsymbol{U}_M(0) + \boldsymbol{V}_M(0). \tag{30}$$

Promote Eq. (30) to $k = 1, 2, \ldots, N$. A data matrix can be obtained as

$$\begin{aligned} &[\boldsymbol{Y}_M(1), \boldsymbol{Y}_M(2), \ldots, \boldsymbol{Y}_M(N)] \\ =& \boldsymbol{\Gamma}_M [\boldsymbol{x}(1), \boldsymbol{x}(2), \ldots, \boldsymbol{x}(N)] \\ &+ \boldsymbol{H}_M [\boldsymbol{U}_M(1), \boldsymbol{U}_M(2), \ldots, \boldsymbol{U}_M(N)] \\ &+ [\boldsymbol{V}_M(1), \boldsymbol{V}_M(2), \ldots, \boldsymbol{V}_M(N)]. \end{aligned} \tag{31}$$

Eq. (31) can be rewritten in a compact form as

$$\boldsymbol{Y} = \boldsymbol{\Gamma}_M \boldsymbol{X} + \boldsymbol{H}_M \boldsymbol{U} + \boldsymbol{V}, \tag{32}$$

by defining

$$\boldsymbol{Y} = [\boldsymbol{Y}_M(1), \boldsymbol{Y}_M(2), \ldots, \boldsymbol{Y}_M(N)], \tag{33}$$
$$\boldsymbol{U} = [\boldsymbol{U}_M(1), \boldsymbol{U}_M(2), \ldots, \boldsymbol{U}_M(N)], \tag{34}$$
$$\boldsymbol{X} = [\boldsymbol{x}(1), \boldsymbol{x}(2), \ldots, \boldsymbol{x}(N)], \tag{35}$$
$$\boldsymbol{V} = [\boldsymbol{V}_M(1), \boldsymbol{V}_M(2), \ldots, \boldsymbol{V}_M(N)]. \tag{36}$$

The noise $\boldsymbol{V}$ can be ignored if the measurement noise is small enough compared to the signal and can be eliminated by filtering. Eq. (32) is then further simplified to

$$\boldsymbol{Y} = \boldsymbol{\Gamma}_M \boldsymbol{X} + \boldsymbol{H}_M \boldsymbol{U}. \tag{37}$$

To eliminate the term $\boldsymbol{U}$ in Eq. (37), a projection matrix is defined as

$$\boldsymbol{\Pi} = \boldsymbol{I} - \boldsymbol{U}^{\mathrm{T}}(\boldsymbol{U}\boldsymbol{U}^{\mathrm{T}})^{-1}\boldsymbol{U} \tag{38}$$

such that $\boldsymbol{U}\boldsymbol{\Pi} = 0$. Thus, multiplying both sides of Eq. (37) by $\boldsymbol{\Pi}$ gives

$$\boldsymbol{O}_M = \boldsymbol{Y}\boldsymbol{\Pi} = \boldsymbol{\Gamma}_M \boldsymbol{X}\boldsymbol{\Pi}. \tag{39}$$

The singular-value decomposition of matrix $\boldsymbol{O}_M$ can be performed as

$$\boldsymbol{O}_M = \boldsymbol{U}_s \boldsymbol{S} \boldsymbol{V}_s^{\mathrm{T}} = \boldsymbol{U}_s \begin{bmatrix} s_1 & 0 & \cdots & 0 \\ 0 & s_2 & \cdots & 0 \\ \vdots & \vdots & & \vdots \\ 0 & 0 & \cdots & s_n \end{bmatrix} \boldsymbol{V}_s^{\mathrm{T}}, \tag{40}$$

where $\boldsymbol{S} \in \mathbb{R}^{n\times n}$, and $s_1, s_2, \ldots, s_n$ are the singular values of $\boldsymbol{O}_M$.

The column space of matrices $\boldsymbol{O}_M$ and $\boldsymbol{\Gamma}_M$ are the same provided that the system is persistently excited and can be derived from Eqs. (39) and (40) as

$$\boldsymbol{\Gamma}_M = \boldsymbol{U}_S, \ \hat{\boldsymbol{X}}\boldsymbol{\Pi} = \boldsymbol{S}\boldsymbol{V}_S^{\mathrm{T}}. \tag{41}$$

Matrices $\boldsymbol{A}$ and $\boldsymbol{C}$ can be estimated directly from $\boldsymbol{\Gamma}_M$, based on the definition in Eq. (25).

Eq. (37) can also be expressed as

$$\boldsymbol{Y}_M = [\boldsymbol{\Gamma}_M, \boldsymbol{C}_{\boldsymbol{B}}, \boldsymbol{C}_{\boldsymbol{D}}] \begin{bmatrix} \boldsymbol{X}(0) \\ \mathrm{vec}(\boldsymbol{B}) \\ \mathrm{vec}(\boldsymbol{D}) \end{bmatrix}, \tag{42}$$

where $\boldsymbol{C}_{\boldsymbol{B}}$ and $\boldsymbol{C}_{\boldsymbol{D}}$ are proportion matrices, defined by

$$\boldsymbol{C}_{\boldsymbol{B}} = \begin{bmatrix} \boldsymbol{0} \\ \boldsymbol{u}^{\mathrm{T}}(1) \otimes \boldsymbol{C} \\ \vdots \\ \sum_{\tau}^{N-2} \left(\boldsymbol{u}^{\mathrm{T}}(1+\tau) \otimes \boldsymbol{C}\boldsymbol{A}^{N-2-\tau}\right) \end{bmatrix},$$
$$\boldsymbol{C}_{\boldsymbol{D}} = \begin{bmatrix} \boldsymbol{u}^{\mathrm{T}}(1) \otimes \boldsymbol{I}_l \\ \boldsymbol{u}^{\mathrm{T}}(2) \otimes \boldsymbol{I}_l \\ \vdots \\ \boldsymbol{u}^{\mathrm{T}}(N) \otimes \boldsymbol{I}_l \end{bmatrix}. \tag{43}$$

The operator '$\otimes$' represents the Kronecker product of two matrices and vec($\boldsymbol{B}$) represents a vector constructed by stacking the columns of matrix $\boldsymbol{B}$ on top of each other. Thus, system matrices $\boldsymbol{B}$ and $\boldsymbol{D}$ and state vector $\boldsymbol{X}(0)$ can be calculated by the linear least-squares method as

$$\begin{bmatrix} \boldsymbol{X}(0) \\ \mathrm{vec}(\boldsymbol{B}) \\ \mathrm{vec}(\boldsymbol{D}) \end{bmatrix} = [\boldsymbol{\Gamma}_M, \boldsymbol{C}_{\boldsymbol{B}}, \boldsymbol{C}_{\boldsymbol{D}}]^{\dagger} \boldsymbol{Y}_N, \tag{44}$$

where $[\boldsymbol{\Gamma}_M, \boldsymbol{C}_{\boldsymbol{B}}, \boldsymbol{C}_{\boldsymbol{D}}]^{\dagger}$ is the generalized inverse matrix of $[\boldsymbol{\Gamma}_M, \boldsymbol{C}_{\boldsymbol{B}}, \boldsymbol{C}_{\boldsymbol{D}}]$.

At this point, system matrices $\boldsymbol{A}$, $\boldsymbol{B}$, $\boldsymbol{C}$, and $\boldsymbol{D}$ are obtained and system output $\boldsymbol{y}(k)$ can be estimated from input $\boldsymbol{u}(k)$.

5 Experimental setup

An experimental setup is built to validate the modeling method (Fig. 3). The structure of the setup follows the design in Fig. 1. A beam emitted from a He-Ne laser (0.8 mW, 632.8 nm, HNR INT-R, LeiChou, China) is reflected by a piezoelectric FSM and projected onto a PSD (S5991-01, Hamamatsu, Japan). The photocurrent of the PSD is amplified by a current-voltage amplifier with four amplification channels and converted to voltage signals. The voltage output is collected by a data acquisition card (PCI-6251, National Instruments, USA). The centroid coordinates of the laser spot in the PSD are calculated by a computer based on four-channel voltage signals. The displacement of the spot is determined by comparing the spot with its nominal position.

The piezoelectric FSM consists of a piezoelectric deflection platform (XS-330.8 SL, XMT Technology, China) and a plane mirror with a diameter

of 25 mm and roughness of $\lambda/4$ (Edmund Optics, USA). The deflection angle of the FSM is in the range of ±6 mrad. An FSM controller (XE509-S3, XMT Technology, China) is used for voltage amplification with an input voltage range of 0–10 V and an output range of 0–150 V.

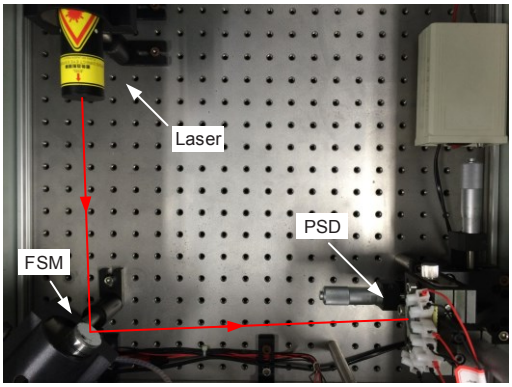

Fig. 3 Photo of the experimental setup. The direction of the laser beam is manipulated by the FSM and the displacement of the spot is measured by the PSD

6 Experiments and results

6.1 Preliminary test

To test the dynamics and coupling of the FSM system, a step voltage is applied to one channel of the FSM with a magnitude of 6 V, while a constant voltage of 5 V is applied to the other input channel. The sampling frequency of the data acquisition card is set to 10 kHz.

The dynamics and coupling of the system are evident in Fig. 4, which shows the displacement of the laser spot with respect to time. Both output channels are affected although the step voltage is applied to only one input channel, which demonstrates the coupling between the input and output channels. Dynamics of the FSM are also clearly visible with a rise time of about 4.9 ms.

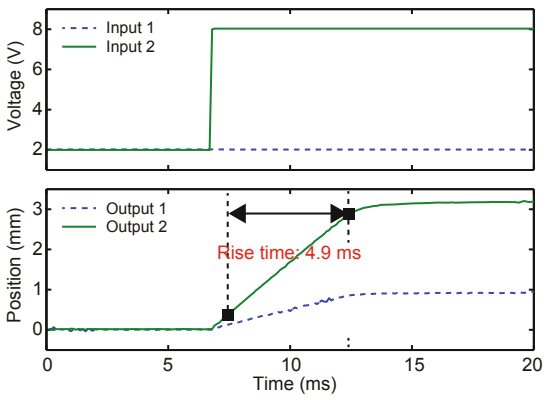

Fig. 4 Step response of the system. Dynamics and coupling are clearly visible

6.2 Model identification and validation

The procedures for model identification and validation are depicted in Fig. 5. Random signals with a magnitude in the range of 4–6 V (Fig. 6) are generated by the computer as the input signal $\boldsymbol{u}(k)$, $k = 1, 2, \ldots, N_1$ ($N_1 = 10^4$) to the FSM. The position of the laser spot in the PSD is collected and the displacement $\boldsymbol{y}(k)$ is calculated. This set of data is referred to as the 'modeling data set'.

Another set of random voltage signals (10^4 samples as well) are generated and used to excite the FSM system and the displacement of the laser spot

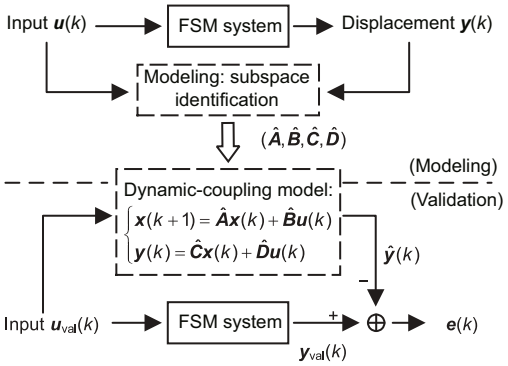

Fig. 5 Flowchart of the modeling and validation process. The system matrices A, B, C, and D are identified by a subspace identification algorithm. The accuracy of the model is evaluated by fresh measurement data

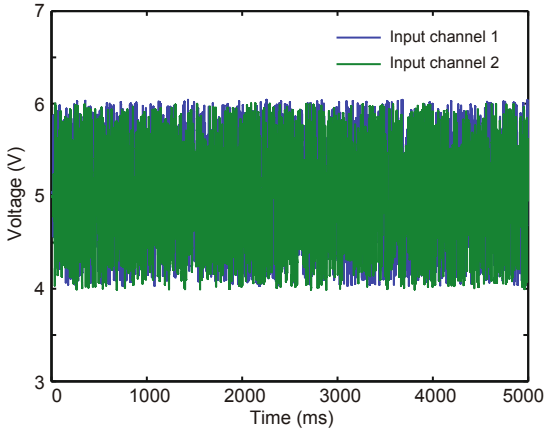

Fig. 6 Signals of two input channels for model identification. The input voltage has a random amplitude in the range of 4–6 V

is collected for validation of the model. This set is called the 'validation data set'.

Based on the modeling data set $\{\boldsymbol{u}(k), \boldsymbol{y}(k)\}_{k=1}^{N_1}$, matrices $\boldsymbol{A}$, $\boldsymbol{B}$, $\boldsymbol{C}$, and $\boldsymbol{D}$ are identified using a subspace identification toolbox (Verhaegen *et al.*, 2007).

To evaluate the accuracy of the model, the variance-accounted-for (VAF) value of the model is calculated as

$$\mathrm{VAF} = \left[1 - \frac{\mathrm{var}(y - \hat{y})}{\mathrm{var}(y)}\right] \times 100\%, \tag{45}$$

where y is from measurement and $\hat{y}$ is the estimated output from the model. The function var$(\cdot)$ denotes the variance of the data sequence. VAF measures the consistency between the model output and the measurement. A greater VAF value indicates a more accurate model of the system (the maximum VAF is 100%).

The system order n is preliminarily determined from the singular values (Fig. 7a) in the singular-value matrix $\boldsymbol{S}$ of Eq. (40). A gap is clearly visible between the second and third singular values and the difference between singular values is negligible beyond the third singular value. Therefore, the system order is preliminarily set to $n = 2$. An optimal model is then selected by comparing VAF values for different orders (Fig. 7b). For $n \geq 2$, VAF values are stable around 97.5%, regardless of the modeling or validation data. This is consistent with the observation in singular values. The estimated system output is compared with measurement and only a small discrepancy exists (Fig. 8), indicating that the system can be modeled accurately by a second-order dynamic model.

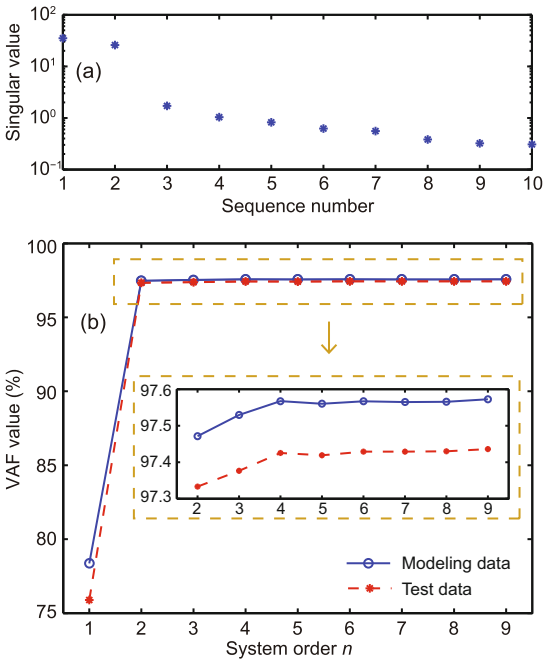

Fig. 7 Determining the system order n by comparing the singular values of matrix $\boldsymbol{S}$ (a) and VAF of the models with different system orders (b). The VAF reaches as high as 97% by a second-order dynamic model

To evaluate the accuracy of the model even further, different signals are applied to test the model and the VAF values are calculated.

Sinusoidal signals are applied to two input channels simultaneously, with the amplitude in the range of 4–6 V. The frequency of the signal is 50 Hz in both channels and the phase difference between two channels is π. The measurements, estimates, and residual are shown in Fig. 9. The VAF value of two channels is 99.82% on average.

Ramp signals are also applied to both channels simultaneously with the amplitude in the range of 2–8 V. Residual are also shown in Fig. 10. The VAF value of two channels is 97.48% on average.

Tests by different signals all indicate that high accuracy is achieved in the model.

6.3 Comparison between dynamic and static models

Based on the input and output data of the modeling data set, a static model is built by linear least-squares fitting as

$$\boldsymbol{D}_s = \boldsymbol{G}\boldsymbol{Q}^{\mathrm{T}}(\boldsymbol{Q}\boldsymbol{Q}^{\mathrm{T}})^{-1}, \tag{46}$$

where $\boldsymbol{D}_s \in \mathbb{R}^{2\times 2}$ is the static model of the system. Matrices $\boldsymbol{G}$ and $\boldsymbol{Q}$ are constructed as

$$\boldsymbol{G} = [\boldsymbol{y}(1), \boldsymbol{y}(2), \ldots, \boldsymbol{y}(N)], \tag{47}$$

$$\boldsymbol{Q} = [\boldsymbol{u}(1), \boldsymbol{u}(2), \ldots, \boldsymbol{u}(N)]. \tag{48}$$

The VAF values for the static model are calculated and compared with those of the dynamic model (Table 1). The VAF for the static model is about 55% for the validation data set, indicating a significant discrepancy between the model estimates and measurement. In contrast, the dynamic model estimates the system output much more accurately, with the VAF better than 97% (an improvement in the VAF of more than 40% compared with the static model).

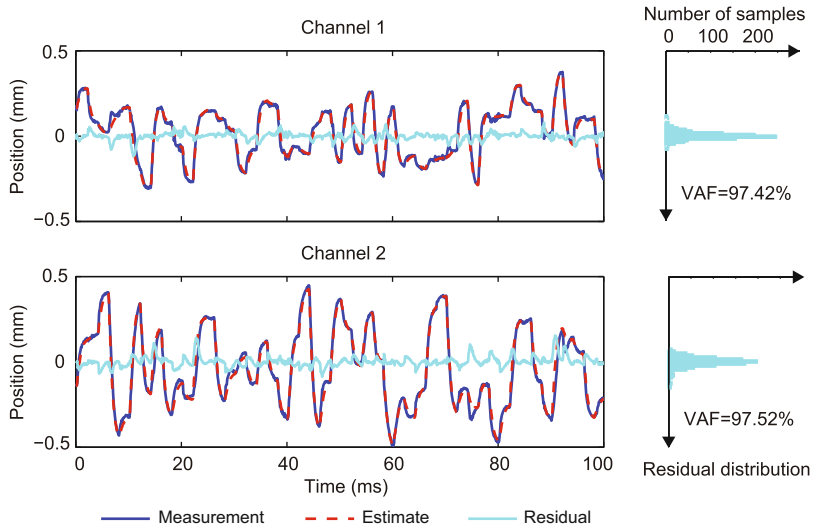

Fig. 8 Comparison between model estimate and measurement in the case of random input signals (only the first 100 ms is plotted). A VAF of more than 97% is achieved for both output channels

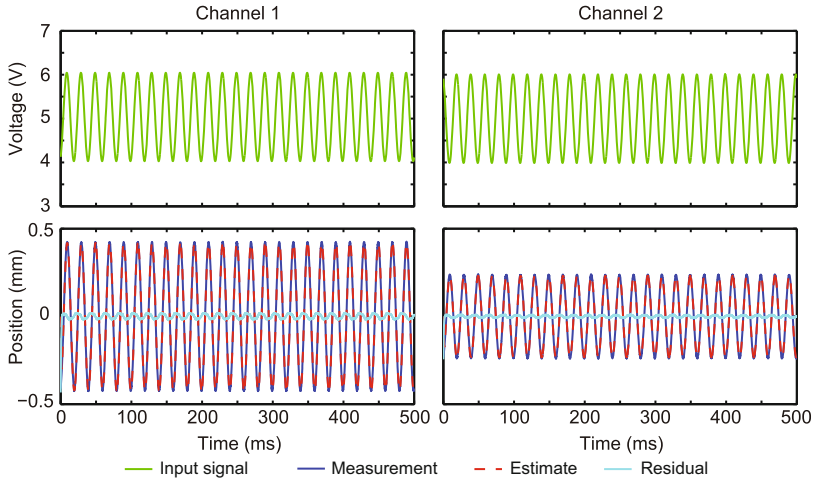

Fig. 9 Comparison between measurements and model estimates in the case of sinusoidal excitations

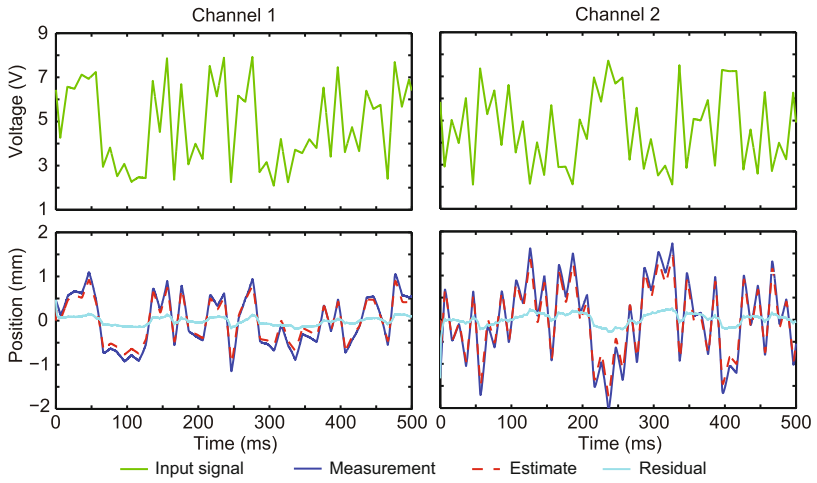

Fig. 10 Comparison between measurements and model estimates in the case of ramp excitations

Therefore, the accuracy of the dynamic model is verified.

Table 1 Comparison of VAF between the dynamic and static models

Model type	VAF (%)	
	Modeling set	Validation set
Static model	57.16	54.97
Dynamic model	97.47	97.33

7 Conclusions

Modeling of an FSM system was discussed, with the dynamics and input-output coupling of the FSM system considered. To achieve high accuracy in the model and to gain insight into the underlying physics, the model was built based on physical principles and identified from input-output data of the system by subspace identification.

Experimental results showed that the VAF values for the dynamic-coupling model are all better than 97%, in the cases of sinusoid, ramp, and random test signals, indicating high accuracy of the model.

Future work will focus on controller design for the closed-loop FSM system.

Acknowledgements

We would like to express sincere gratitude to Dr. M. VERHAEGEN from Delft University of Technology for supporting the toolbox for subspace identification.

References

Alvi, B.A., Asif, M., Siddiqui, F.A., *et al.*, 2014. Fast steering mirror control using embedded self-learning fuzzy controller for free space optical communication. *Wirel. Pers. Commun.*, **76**(3):643-656. https://doi.org/10.1007/s11277-014-1731-1

Arancibia, N.O.P., Chen, N., Gibson, S., *et al.*, 2006. Adaptive control of a MEMS steering mirror for suppression of laser beam jitter. Proc. American Control Conf., Article 104206. https://doi.org/10.1109/ACC.2005.1470530

Cao, Z.L., Mu, Q.Q., Hu, L.F., *et al.*, 2009. Preliminary use of nematic liquid crystal adaptive optics with a 2.16-meter reflecting telescope. *Opt. Expr.*, **17**(4):2530-2537. https://doi.org/10.1364/OE.17.002530

Cao, Z.L., Mu, Q.Q., Hu, L.F., *et al.*, 2012. Optimal energy-splitting method for an open-loop liquid crystal adaptive optics system. *Opt. Expr.*, **20**(17):19331-19342. https://doi.org/10.1364/OE.20.019331

Chiuso, A., Muradore, R., Marchetti, E., 2010. Dynamic calibration of adaptive optics systems: a system identification approach. *IEEE Trans. Contr. Syst. Technol.*, **18**(3):705-713. https://doi.org/10.1109/TCST.2009.2023914

Hei, M., Zhang, L.C., Zhou, Q.K., *et al.*, 2015. Model-based design method of two-axis four-actuator fast steering mirror system. *J. Centr. South Univ.*, **22**(1):150-158. https://doi.org/10.1007/s11771-015-2505-y

Hinnen, K., Verhaegen, M., Doelman, N., 2008. A data-driven $\mathcal{H}_2$-optimal control approach for adaptive optics. *IEEE Trans. Contr. Syst. Technol.*, **16**(3):381-395. https://doi.org/10.1109/TCST.2007.903374

Jansson, M., Wahlberg, B., 1996. A linear regression approach to state-space subspace system identification. *Signal Process.*, **52**(2):103-129. https://doi.org/10.1016/0165-1684(96)00048-5

Lu, Y.F., Fan, D.P., Zhang, Z.Y., 2013. Theoretical and experimental determination of bandwidth for a two-axis fast steering mirror. *Opt. Int. J. Light Electron Opt.*, **124**(16):2443-2449. https://doi.org/10.1016/j.ijleo.2012.08.023

Mu, Q.Q., Cao, Z.L., Li, C., *et al.*, 2008. Accommodation-based liquid crystal adaptive optics system for large ocular aberration correction. *Opt. Lett.*, **33**(24):2898-2900. https://doi.org/10.1364/OL.33.002898

Portillo, A.A., Ortiz, G.G., Racho, C., 2001. Fine pointing control for optical communications. Proc. IEEE Aerospace Conf., 1541-1550. https://doi.org/10.1109/AERO.2001.931385

Raj, A.A.B., Selvi, J.A.V., Kumar, D., *et al.*, 2015. Design of cognitive decision making controller for autonomous online adaptive beam steering in free space optical communication system. *Wirel. Pers. Commun.*, **84**(1):765-799. https://doi.org/10.1007/s11277-015-2660-3

Song, H., Fraanje, R., Schitter, G., *et al.*, 2011. Controller design for a high-sampling-rate closed-loop adaptive optics system with Piezo-driven deformable mirror. *Eur. J. Contr.*, **17**(3):290-301. https://doi.org/10.3166/ejc.17.290-301

Tang, T., Ma, J.G., Ge, R., 2011. PID-I controller of charge coupled device-based tracking loop for fast-steering mirror. *Opt. Eng.*, **50**(4):043002. https://doi.org/10.1117/1.3567059

Verhaegen, M., Verdult, V., 2007. Filtering and System Identification: a Least Squares Approach. Cambridge University Press, Cambridge.

Verhaegen, M., Verdult, V., Bergboer, N., 2007. Filtering and System Identification: an Introduction to Using Matlab Software. Delft University of Technology, the Netherlands.

Wang, G., Rao, C.H., 2015. Adaptive control of piezoelectric fast steering mirror for high precision tracking application. *Smart Mater. Struct.*, **24**(3):035019. https://doi.org/10.1088/0964-1726/24/3/035019

Yu, Z.L., Cui, N., Chen, X.L., *et al.*, 2015. H_∞ control for fast steering mirror based on the incremental PI controller. Proc. Conf. of the Photoelectronic Technology Committee of the Chinese Society of Astronautics, Article 95210G. https://doi.org/10.1117/12.2087306